Non-Gaussian distribution and clustering of hot and cold pixels in the five-year *WMAP* sky

Graziano Rossi,[1]⋆ Ravi K. Sheth,[2] Changbom Park[1]
and Carlos Hernández-Monteagudo[3]

[1]*Korea Institute for Advanced Study, Hoegiro 87, Dongdaemun-Gu, Seoul 130-722, Korea*
[2]*Department of Physics and Astronomy, University of Pennsylvania, 209 South 33rd Street, Philadelphia, PA 19104-6396, USA*
[3]*Max-Planck-Institut fuer Astrophysik, Karl-Schwarzschild Str. 1, D-85741 Garching bei Muenchen, Germany*

ABSTRACT

We present measurements of the clustering of hot and cold patches in the microwave background sky as measured from the *Wilkinson Microwave Anisotropy Probe* 5-year data. These measurements are compared with theoretical predictions which assume that the cosmological signal obeys Gaussian statistics. We find significant differences from the simplest Gaussian-based prediction. However, the measurements are sensitive to the fact that the noise is spatially inhomogeneous (e.g. because different parts of the sky were observed for different lengths of time). We show how to account for this spatial inhomogeneity when making predictions. Differences from the Gaussian-based expectation remain even after this more careful accounting of the noise. In particular, we note that hot and cold pixels cluster differently within the same temperature thresholds at few-degree scales. While these findings may indicate primordial non-Gaussianity, we discuss other plausible explanations for these discrepancies. In addition, we find some deviations from Gaussianity at sub-degree scales, especially in the *W* band, whose origin may be associated with extragalactic dust emission.

Key words: methods: data analysis – methods: statistical – cosmic microwave background – cosmology: observations – early Universe – Large-scale structure of Universe.

1 INTRODUCTION

Non-Gaussianity of the cosmic microwave background (CMB) is progressively becoming a crucial probe of the inflationary dynamics, since models beyond single-field slow-roll inflation predict large distinct non-Gaussianities above the current limit of measurement (Lyth, Ungarelli & Wands 2003; Lyth & Riotto 2006; Bartolo et al. 2004; Dvali, Gruzinov & Zaldarriaga 2004; Chen 2005; Seery & Lidsey 2005; Chen & Szapudi 2006; Seery & Hidalgo 2006; Ling & Wu 2009; Senatore, Tassev & Zaldarriaga 2008; Senatore, Smith & Zaldarriaga 2009; Chen et al. 2009). Moreover, up to date a number of plausible alternative early universe models also predict skewed primordial fluctuations, and are in principle distinguishable from other scenarios through the shape dependence of high-order correlation functions (Alishahiha, Silverstein & Tong 2004; Arkani-Hamed et al. 2004; Creminelli & Senatore 2007; Brandenberger 2008; Buchbinder, Khoury & Ovrut 2008; Lehners & Steinhardt 2008; McAllister & Silverstein 2008).

An even small degree of primordial non-Gaussianity would indicate a quite different structure formation scenario from the con-

cordance cosmological model in which density perturbations are assumed to be a Gaussian random field, and alter significantly the statistics of voids (e.g. Kamionkowski, Verde & Jimenez 2009; Song & Lee 2008). Imprints of primordial non-Gaussianity can manifest in the statistical properties of the Lyman-α forest quasi-stellar object spectra at intermediate redshift (Viel et al. 2009), in the large-scale distribution of neutral hydrogen (Pillepich, Porciani & Matarrese 2007), in the reionization history of the Universe (Crociani et al. 2009) and in the abundance, clustering and biasing of dark matter haloes (Kang, Norberg & Silk 2007; Carbone, Verde & Matarrese 2008; Dalal et al. 2008; Desjacques, Seljak & Iliev 2008; Grossi et al. 2008; Lo Verde et al. 2008; Matarrese & Verde 2008; McDonald & Seljak 2008; Pillepich, Porciani & Hahn 2008; Seljak 2009; Slosar et al. 2008; Jeong & Komatsu 2009). Topology of the large-scale structure is also very sensitive to the initial conditions of the matter density field, and potentially represents a strong and independent test of deviations from the Gaussian hypothesis (Park et al. 1998; Park, Gott & Choi 2001; Park et al. 2005; Gott et al. 2008, 2009; Hikage et al. 2008b).

Hence, there is significant interest in quantifying the Gaussianity of the cosmic background radiation, and a multitude of non-Gaussian estimators have been applied so far. In particular, data from the *Wilkinson Microwave Anisotropy Probe* (*WMAP*)

⋆E-mail: graziano@kias.re.kr

mission has been used to constrain primordial non-Gaussianity. Recent measurements of the one- and three-point probability functions, the bispectrum and trispectrum, the genus statistic and the other Minkowski functionals (Cabella et al. 2005; Hinshaw et al. 2007; Creminelli et al. 2007; Gott et al. 2007; Spergel et al. 2007; Curto et al. 2009; Hikage et al. 2008a; Hinshaw et al. 2009; Komatsu et al. 2009; Vielva & Sanz 2009; Pietrobon et al. 2009a) from the first 3 or 5 years of *WMAP* data are all consistent with Gaussianity. However, a considerable number of anomalies like asymmetries, intrinsic alignments in the data or the presence of unusual cold spots have also been reported (Cruz et al. 2006; Tojeiro et al. 2006; Chiang, Naselsky & Coles 2007; Naselsky et al. 2007; Räth, Schuecker & Banday 2007; Vielva et al. 2007; Hansen et al. 2008; Dickinson et al. 2009; Diego et al. 2009; Li et al. 2009; Pietrobon et al. 2009b; Räth et al. 2009; Rossmanith et al. 2009), as well as some claims of non-Gaussianity (Jeong & Smoot 2007; Yadav & Wandelt 2008), which, if confirmed, would rule out a large class of inflationary models.

In this paper, we investigate the Gaussian hypothesis using the clustering statistics of pixels that lie above or below a threshold. For a Gaussian field, the scale dependence of this statistic and its dependence on threshold have been predicted (Jensen & Szalay 1986). It turns out that a careful accounting for the effects of noise is crucial to perform this test. Kashlinsky, Hernández-Monteagudo & Atrio-Barandela (2001) and Hernández-Monteagudo, Kashlinsky & Atrio-Barandela (2004) presented an analysis of the problem when the noise is spatially homogeneous. In the case of *WMAP*, the noise is spatially inhomogeneous; the present work shows how to incorporate this complexity into the analysis.

The layout of the paper is as follows. In Section 2, we outline the theoretical framework for the two-point statistics above a temperature threshold, and show how to incorporate the complexity of inhomogeneous noise into the two-point formalism. Some details on error-bar calculations are left in Appendix A. In Section 3, we test our theory against *WMAP* 5-year data. We study and quantify the inhomogeneous noise properties and show that the abundance and clustering of pixels (both scale and dependence on threshold temperature) appear to be inconsistent with the Gaussian prediction if one ignores the fact that the noise is spatially inhomogeneous. We compare the number density of pixels above threshold and the one- and two-point statistics measurements with the theory, allowing for inhomogeneous noise. While this improves the agreement between measurements and predictions, discrepancies remain. Although this may be an indication of primordial non-Gaussianity, we discuss a variety of other possibilities, among which the effect of smoothing the map. We inspect all the *WMAP* 5-year channels, but we present in the main text results only for the W1 differencing assembly (DA), and leave in Appendix B results for other DAs. A final section summarizes our findings, and highlights ongoing and future studies.

2 THEORETICAL MODEL

2.1 Basic notation

Denote the observed value in a pixel by $D = T - \langle T \rangle \equiv \delta T$, which is the sum of the true signal s plus noise n, both of which have mean zero. We consider a model in which the signal is homogeneous and may have spatial correlations whereas the noise, which is independent of the signal, may be inhomogeneous and have spatial correlations. By this, we mean that the rms value of the noise σ_n may fluctuate from pixel to pixel and these fluctuations

may be correlated, and that the actual value of the noise in one pixel could depend on that in another. Let $p(D)$ denote the observed one-point distribution of D, $G(s)$ the distribution of s, $p(\sigma_n)$ the distribution of the rms value of the noise in a pixel and $g(n|\sigma_n)$ the distribution of the noise when the rms value of the noise is σ_n. Note that $g(n) = \int g(n|\sigma_n) p(\sigma_n) d\sigma_n$. Our convention is to use capital letters for average quantities, and lower case letters for actual (varying) quantities. Later on in the paper we will also drop the (understood) subscript 'n' of the rms of the noise, for clarity of notation.

2.2 One-point observed distribution

Since the distribution of the noise $g(n)$ is independent of the signal s,

$$
\begin{aligned}
p(D) &= \int ds\, G(s) \int dn\, g(n) \delta_D(s + n = D) \\
&= \int ds\, G(s) \int dn \int d\sigma_n\, g(n \mid \sigma_n)\, p(\sigma_n) \\
&\quad \times \delta_D(s + n = D) \\
&= \int d\sigma_n\, p(\sigma_n) \int ds\, G(s)\, g(D - s \mid \sigma_n) \\
&= \int d\sigma_n\, p(\sigma_n)\, p(D \mid \sigma_n),
\end{aligned}
\tag{1}
$$

where δ_D is the Dirac delta and

$$
p(D \mid \sigma_n) = \int ds\, G(s)\, g(D - s \mid \sigma_n).
\tag{2}
$$

The variance of D is

$$
\begin{aligned}
\sigma_D^2 &\equiv \langle D^2 \rangle = \int dD\, p(D)\, D^2 \\
&= \int d\sigma_n\, p(\sigma_n) \int ds\, G(s) \int dn\, g(n \mid \sigma_n)(s + n)^2 \\
&= \sigma_S^2 + \int d\sigma_n\, p(\sigma_n) \langle n^2 \mid \sigma_n \rangle \\
&= \sigma_S^2 + \sigma_N^2,
\end{aligned}
\tag{3}
$$

where we have used σ_S to denote the rms value of the signal and σ_N^2 to denote the variance of the noise upon averaging over all pixels. It is also straightforward to show that $\langle D \rangle = 0$, as expected.

The fraction of pixels above some threshold D_t is

$$
\begin{aligned}
f(D_t) &= \int_{D_t}^{\infty} dD\, p(D) = \int d\sigma_n\, p(\sigma_n) \int_{D_t}^{\infty} dD\, p(D \mid \sigma_n) \\
&= \int d\sigma_n\, p(\sigma_n)\, f(D_t \mid \sigma_n).
\end{aligned}
\tag{4}
$$

If $\langle D | D_t \rangle$ denotes the mean value of D in such pixels then

$$
\begin{aligned}
f(D_t) \langle D \mid D_t \rangle &= \int_{D_t}^{\infty} dD\, p(D)\, D \\
&= \int d\sigma_n\, p(\sigma_n) \int_{D_t}^{\infty} dD\, p(D \mid \sigma_n)\, D \\
&= \int d\sigma_n\, p(\sigma_n)\, f(D_t \mid \sigma_n) \langle D \mid D_t, \sigma_n \rangle.
\end{aligned}
\tag{5}
$$

2.3 Two-point observed distribution

Two-point statistics may be computed similarly. For two pixels separated by the angular distance θ,

$$
\begin{aligned}
p(D_1, D_2 \mid \theta) &= \int ds_1 \int ds_2 \, G(s_1, s_2 \mid \theta) \int dn_1 \int dn_2 \\
&\quad \times g(n_1, n_2) \, \delta_D(s_1 + n_1 = D_1) \, \delta_D(s_2 + n_2 = D_2) \\
&= \int ds_1 \int ds_2 \, G(s_1, s_2 \mid \theta) \int dn_1 \int dn_2 \int d\sigma_1 \\
&\quad \times \int d\sigma_2 \, g(n_1, n_2 \mid \sigma_1, \sigma_2) \, p(\sigma_1, \sigma_2 \mid \theta) \, \delta_D(s_1 + n_1 = D_1) \\
&\quad \times \delta_D(s_2 + n_2 = D_2) \\
&= \int d\sigma_1 \int d\sigma_2 \, p(\sigma_1, \sigma_2 \mid \theta) \int ds_1 \int ds_2 \, G(s_1, s_2 \mid \theta) \\
&\quad \times g(D_1 - s_1 \mid \sigma_1) \, g(D_2 - s_2 \mid \sigma_2) \\
&= \int d\sigma_1 \int d\sigma_2 \, p(\sigma_1, \sigma_2 \mid \theta) \, p(D_1, D_2 \mid \sigma_1, \sigma_2, \theta),
\end{aligned}
\tag{6}
$$

where

$$
\begin{aligned}
p(D_1, D_2 \mid \sigma_1, \sigma_2, \theta) &= \int ds_1 \int ds_2 \, G(s_1, s_2 \mid \theta) \\
&\quad \times g(D_1 - s_1 \mid \sigma_1) \, g(D_2 - s_2 \mid \sigma_2).
\end{aligned}
\tag{7}
$$

Note that if we integrate over all pixels then

$$
\begin{aligned}
\langle D_1 D_2 \mid \theta \rangle &= \int dD_1 \int dD_2 \, D_1 D_2 \, p(D_1, D_2 \mid \theta) \\
&= \int ds_1 \int ds_2 \, G(s_1, s_2 \mid \theta) \, s_1 s_2 \\
&\quad + \int dn_1 \int dn_2 \, g(n_1, n_2 \mid \theta) \, n_1 n_2 \\
&= \langle s_1 s_2 \mid \theta \rangle + \langle n_1 n_2 \mid \theta \rangle \\
&\equiv C_S(\theta) + C_N(\theta) = C(\theta),
\end{aligned}
\tag{8}
$$

where

$$
\langle s_1 s_2 \mid \theta \rangle = \int ds_1 \int ds_2 \, G(s_1, s_2 \mid \theta) \, s_1 s_2 \equiv C_S(\theta)
\tag{9}
$$

and

$$
\begin{aligned}
\langle n_1 n_2 \mid \theta \rangle &= \int dn_1 \int dn_2 \, g(n_1, n_2 \mid \theta) \, n_1 n_2 \\
&= \int dn_1 \int dn_2 \int_0^\infty d\sigma_1 \int_0^\infty d\sigma_2 \, p(\sigma_1, \sigma_2 \mid \theta) \\
&\quad \times g(n_1, n_2 \mid \sigma_1, \sigma_2, \theta) \, n_1 n_2 \\
&= \int_0^\infty d\sigma_1 \int_0^\infty d\sigma_2 \, p(\sigma_1, \sigma_2 \mid \theta) \int dn_1 \int dn_2 \\
&\quad \times g(n_1, n_2 \mid \sigma_1, \sigma_2, \theta) \, n_1 n_2 \\
&= \int_0^\infty d\sigma_1 \int_0^\infty d\sigma_2 \, p(\sigma_1, \sigma_2 \mid \theta) \, \langle n_1 n_2 \mid \sigma_1, \sigma_2, \theta \rangle \\
&\equiv C_N(\theta).
\end{aligned}
\tag{10}
$$

This is because the signal and noise are uncorrelated, and so $\langle sn \mid \theta \rangle = 0$ for all $\theta > 0$. Clearly, if the noise is not spatially correlated then $\langle n_1 n_2 \mid \theta \rangle = 0$ and $\langle D_1 D_2 \mid \theta \rangle \equiv C_S(\theta)$.

If the rms values of the noise are perfectly correlated, meaning $\sigma_1 = \sigma_2$, then it is convenient to write $p(\sigma_1, \sigma_2 \mid \theta) = p(\sigma_1) \, p(\sigma_2 \mid \sigma_1, \theta)$ and replace $p(\sigma_2 \mid \sigma_1, \theta)$ with a delta function centred on $\sigma_1 = $

σ_n. One then averages over the distribution of σ_n, namely

$$
\begin{aligned}
p(D_1, D_2 \mid \theta) &= \int d\sigma_1 \int d\sigma_2 \, p(\sigma_1) \, \delta_D(\sigma_1 = \sigma_2 \equiv \sigma_n) \\
&\quad \times p(D_1, D_2 \mid \sigma_1, \sigma_2, \theta) \\
&= \int d\sigma_n \, p(\sigma_n) \, p(D_1, D_2 \mid \sigma_n, \sigma_n, \theta).
\end{aligned}
\tag{11}
$$

If, in addition, one replaces $p(\sigma_n)$ with a delta function centred on σ_N then $p(D_1, D_2 \mid \theta) \equiv p(D_1, D_2 \mid \sigma_N, \sigma_N, \theta)$, and the homogeneous case is recovered. The noise distributions $p(\sigma_n)$ and $p(\sigma_1, \sigma_2 \mid \theta)$ are measured directly from the *WMAP* 5-year data.

2.4 Two-point function above threshold and inhomogeneous noise

The two-point unweighted correlation function $\xi(\theta)$ estimates the excess of probability of finding a pair at a distance θ, compared to a random catalogue (e.g. Jensen & Szalay 1986). Similarly, one can define the two-point weighted correlation function $W(\theta)$, which differs from $\xi(\theta)$ only because each member of the pair is now weighted by some (average) mark. In this study, the mark is given by $\delta T / \langle \delta T \rangle \equiv D / \langle D \rangle$. Two-point correlation functions of regions above some threshold are readily obtained by integration above the threshold level.

Within the formalism previously outlined, the two-point correlation function of pixels above some threshold D_t is

$$
1 + \xi_t(\theta) = \int_{D_t}^\infty dD_1 \int_{D_t}^\infty dD_2 \, \frac{p(D_1, D_2 \mid \theta)}{f(D_t)^2}
\tag{12}
$$

and the associated weighted function is

$$
1 + W_t(\theta) = \int_{D_t}^\infty dD_1 \int_{D_t}^\infty dD_2 \, \frac{D_1 D_2}{\langle D \mid D_t \rangle^2} \, \frac{p(D_1, D_2 \mid \theta)}{f(D_t)^2},
\tag{13}
$$

where $p(D_1, D_2 \mid \theta)$, $\langle D \mid D_t \rangle$ and $f(D_t)$ have been previously defined.

To gain intuition, it is helpful to define

$$
1 + \xi_t(\theta \mid \sigma_1, \sigma_2) = \int_{D_t}^\infty dD_1 \int_{D_t}^\infty dD_2 \, \frac{p(D_1, D_2 \mid \sigma_1, \sigma_2, \theta)}{f(D_t \mid \sigma_1) f(D_t \mid \sigma_2)}
\tag{14}
$$

and

$$
\begin{aligned}
1 + W_t(\theta \mid \sigma_1, \sigma_2) &= \int_{D_t}^\infty dD_1 \int_{D_t}^\infty dD_2 \, \frac{D_1 D_2}{\langle D \mid D_t, \sigma_1 \rangle \langle D \mid D_t, \sigma_2 \rangle} \\
&\quad \times \frac{p(D_1, D_2 \mid \sigma_1, \sigma_2, \theta)}{f(D_t \mid \sigma_1) f(D_t \mid \sigma_2)},
\end{aligned}
\tag{15}
$$

in terms of which

$$
\begin{aligned}
1 + \xi_t(\theta) &= \int d\sigma_1 \int d\sigma_2 \, p(\sigma_1, \sigma_2 \mid \theta) \, \frac{f(D_t \mid \sigma_1) f(D_t \mid \sigma_2)}{f(D_t)^2} \\
&\quad \times \left[1 + \xi_t(\theta \mid \sigma_1, \sigma_2) \right]
\end{aligned}
\tag{16}
$$

and

$$
\begin{aligned}
1 + W_t(\theta) &= \int d\sigma_1 \int d\sigma_2 \, p(\sigma_1, \sigma_2 \mid \theta) \frac{f(D_t \mid \sigma_1) \langle D \mid D_t, \sigma_1 \rangle}{f(D_t) \langle D \mid D_t \rangle} \\
&\quad \times \frac{f(D_t \mid \sigma_2) \langle D \mid D_t, \sigma_2 \rangle}{f(D_t) \langle D \mid D_t \rangle} \left[1 + W_t(\theta \mid \sigma_1, \sigma_2) \right].
\end{aligned}
\tag{17}
$$

This shows that ξ_t and W_t can be thought of as weighted averages over the values at fixed σ_1 and σ_2. This rewriting shows clearly that the key quantity of interest are $p(D_1, D_2 \mid \sigma_1, \sigma_2, \theta)$, which is the convolution of the signal and noise distributions, and $p(D \mid \sigma_n)$. This rewriting also allows one to study two limiting cases.

If the rms values of the noise are perfectly correlated, meaning $\sigma_1 = \sigma_2 \equiv \sigma_n$, then

$$1 + \xi_t(\theta) = \int d\sigma_n \, p(\sigma_n) \int_{D_t}^{\infty} dD_1 \int_{D_t}^{\infty} dD_2$$
$$\times \frac{p(D_1, D_2 \mid \sigma_n, \sigma_n, \theta)}{f(D_t)^2} \qquad (18)$$

and

$$1 + W_t(\theta) = \int d\sigma_n \, p(\sigma_n) \int_{D_t}^{\infty} dD_1 \int_{D_t}^{\infty} dD_2 \frac{D_1 D_2}{\langle D \mid D_t \rangle^2}$$
$$\times \frac{p(D_1, D_2 \mid \sigma_n, \sigma_n, \theta)}{f(D_t)^2}. \qquad (19)$$

If, in addition, one replaces $p(\sigma_n)$ with a delta function centred on σ_N then

$$1 + \xi_t(\theta) = \int_{D_t}^{\infty} dD_1 \int_{D_t}^{\infty} dD_2 \frac{p(D_1, D_2 \mid \sigma_N, \sigma_N, \theta)}{f(D_t)^2} \qquad (20)$$

and

$$1 + W_t(\theta) = \int_{D_t}^{\infty} dD_1 \int_{D_t}^{\infty} dD_2 \frac{D_1 D_2}{\langle D \mid D_t \rangle^2}$$
$$\times \frac{p(D_1, D_2 \mid \sigma_N, \sigma_N, \theta)}{f(D_t)^2}. \qquad (21)$$

We are particularly interested in the case where the signal $G(s_1, s_2 \mid \theta)$ is bivariate Gaussian with $\langle s_1^2 \rangle = \langle s_2^2 \rangle = \sigma_S^2$ and $\langle s_1 s_2 \mid \theta \rangle = C_S(\theta)$, and the noise $g(n \mid \sigma_n)$ is Gaussian with rms σ_n. Then,

$$p(D_1, D_2 \mid \sigma_1, \sigma_2, \theta) = \frac{1}{2\pi\sqrt{\|C\|}} e^{-\frac{1}{2} D^T C^{-1} D}$$
$$= \frac{1}{2\pi\sigma_D^2 \sqrt{\alpha_1 \alpha_2 - w_\theta^2}} \exp\left[-\frac{\alpha_2 D_1^2 + \alpha_1 D_2^2 - 2w_\theta \, D_1 D_2}{2\sigma_D^2 (\alpha_1 \alpha_2 - w_\theta^2)} \right], \qquad (22)$$

with $\alpha_1 = (\sigma_S^2 + \sigma_1^2)/\sigma_D^2$, $\alpha_2 = (\sigma_S^2 + \sigma_2^2)/\sigma_D^2$ and

$$w_\theta = \frac{C_S(\theta) + C_N(\theta)}{\sigma_D^2}, \qquad (23)$$

$$C_S(\theta) = \sum_\ell \frac{(2\ell+1)}{4\pi} C_\ell \, W_\ell^{WMAP} \, W_\ell^{smooth} \, P_\ell^0(\cos\theta), \qquad (24)$$

$$C_N(\theta) = \sum_\ell \frac{(2\ell+1)}{4\pi} C_\ell^N \, W_\ell^{smooth} \, P_\ell^0(\cos\theta), \qquad (25)$$

where C is the covariance matrix of the temperature field, C_ℓ^N is the power spectrum of the noise map, W^{WMAP} is the *WMAP* window function and W^{smooth} is the additional smoothing due to finite pixel size, mask influence and an optional additional Gaussian beam smoothing.

If the noise is spatially uncorrelated then clearly $C_N(\theta) = 0$ and therefore $w_\theta \equiv C_S(\theta)/\sigma_D^2$.

In the approximation where $\sigma_1 = \sigma_2$, rms noise varies spatially on scales much larger than those of interest, then $\alpha_1 = \alpha_2$. The 'standard' approximation, rms noise independent of position, has $\alpha_1 = \alpha_2 = 1$ and we recover the Hernández-Monteagudo et al. (2004) formula.

Uncertainties in the correlation functions above threshold are estimated from the optimal variance limit, containing cosmic variance, instrumental noise (Knox 1995; Hernández-Monteagudo et al. 2004) and finite bin-size effects (see Appendix A for more details).

3 ANALYSIS OF *WMAP* 5-YEAR DATA

3.1 Data set and pipeline

The data from the 5 years of the *WMAP* mission are available online at Legacy Archive for Microwave Background DAta (LAMBDA) website (http://lambda.gsfc.nasa.gov/), NASA's CMB Thematic Data Center. For the purposes of this study, we use the *WMAP* 5-year full-resolution 'foreground-reduced' coadded sky maps (produced by performing a weighted pixel-by-pixel mean of the five single-year maps; see Hinshaw et al. 2009) for the W (the 94 GHz channel), V (the 61 GHz channel) and Q (the 41 GHz channel) DAs. We show results for the W1 channel in the main text, and leave in Appendix B major results for all the other individual DAs. The data consist of four fields for each pixel:

(i)   the thermodynamic temperature in mK,
(ii) the Q polarization temperature in mK,
(iii) the U polarization temperature in mK and
(iv) the effective number of observations, N_{obs}.

The maps are provided in the HEALPIX scheme (Górski et al. 1999) at a resolution of $N_{side} = 512$, giving a total of 3 145 728 pixels separated on average by $\theta_{pix} = 6.87$ arcmin. The maps have been cleaned of Galactic foreground emission using external templates, as explained in Gold et al. (2009). It is indeed necessary to mask out regions of strong foreground emission. Of the different masks provided from the LAMBDA Legacy Archive, which allow for the selective exclusion of portions of the sky at different flux levels, we chose the most conservative, KQ75 – essentially an extension and improvement of the standard KP0 cut in the 3-year data release. This choice removes about 28 per cent of the pixels. Point sources are masked based on a combination of external catalogue data and *WMAP*-detected sources (Wright et al. 2009). Note that point sources are the largest astrophysical contaminant to the temperature power spectrum.

Our theory predictions (Section 2) depend on the temperature (TT) power spectrum, on the shape of the *WMAP* beam and on the noise properties. We used the beam and window transfer functions from the 5-year *WMAP* data, which have been significantly improved with the 5-year data release; models of the instrument gain and beam response are now accurate to better than $\sim$0.6 per cent, and errors in the 5-year beam transfer functions are reduced by a factor of $\sim$2 as compared to the 3-year analysis (Hill et al. 2009). The *WMAP*5 TT power spectrum we use comes from a weighted combination of 153 individual cross-power spectra, and has been improved by using a Gibbs-based maximum likelihood estimate for $l \leq 32$ (Dunkley et al. 2008) and a pseudo-C_ℓ estimate for higher l (Nolta et al. 2009). The pixel–pixel covariance matrix is essentially diagonal (Hinshaw et al. 2003; Hinshaw et al. 2009), so the rms noise in pixel p is $\sigma(p) = \sigma_0/\sqrt{N_{obs}(p)}$, where the noise per observation, σ_0, is provided for each coadded channel. This value for σ_0 is obtained by averaging the values of the five possible year-by-year difference combinations (Jarosik et al. 2007; Hinshaw et al. 2009).

The data reduction process should be free of contamination induced by foregrounds, and should be insensitive to monopole and dipole moments. At $N_{side} = 512$, the generic data pipeline involves the following main steps:

(i)   dipole and monopole removal outside KQ75;
(ii) selection of pixels above a temperature threshold;
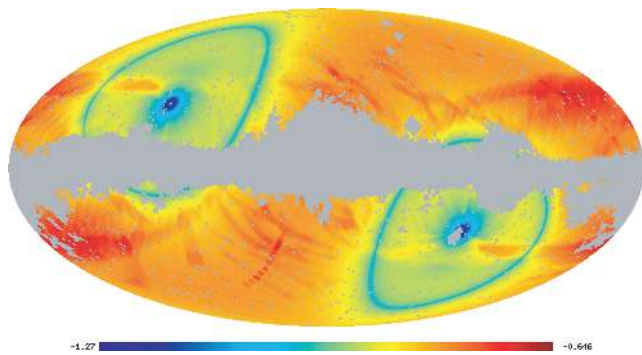(iii) HEALPIX coordinate and pixel-noise assignment.

Figure 1. Noise per pixel distribution at $N_{side} = 512$ for the 5-year coadded *WMAP* data (W1 channel), after application of the KQ75 mask, in the Mollweide projection. The scale is logarithmic, in mK units – i.e. $\log_{10}(\sigma_n)$ is shown.
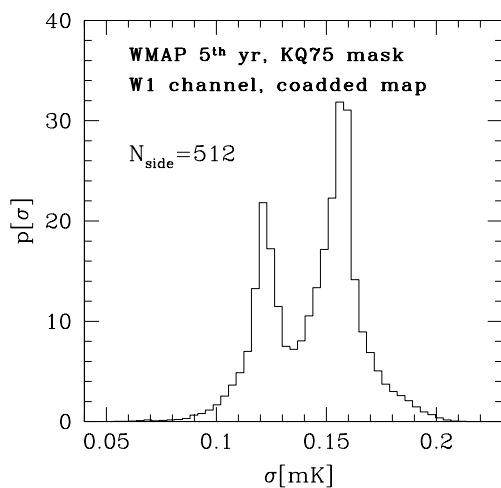

Figure 2. Distribution of the rms noise per pixel at $N_{side} = 512$ for the *WMAP*5 W1 coadded channel, after application of the KQ75 mask.

3.2 Inhomogeneous noise properties

The distribution of the rms noise values in a pixel at $N_{side} = 512$ is shown in the Mollweide projection in Fig. 1, and as histogram in Fig. 2, for the *WMAP*5 W1 channel. The distribution is reasonably broad, indicating that the noise is inhomogeneous. This is a direct consequence of the fact that not all pixels were observed the same number of times. The evident symmetrical pattern present in Fig. 1 is due to the scanning strategy of the *WMAP* satellite.

In particular, equations (16) and (17) show that the clustering of pixels separated by θ depends on the joint distribution of $p(\sigma_1, \sigma_2)$ given θ. Fig. 3 shows an example of how the joint distribution $p(\sigma_1, \sigma_2|\theta)$ varies as a function of separation θ for the resolution $N_{side} = 512$. The four panels were constructed by randomly selecting 1000 pixels, and for each selected value of σ_1, looking at the corresponding σ_2 distributions at four different angular distances. Note that the scatter around the one-to-one line increases with increasing θ. This is not surprising; nearby pixels have similar N_{obs} whereas more widely separated ones do not (Fig. 1). Fig. 4 shows some examples of the corresponding conditional distributions $p(\sigma_2|\sigma_1, \theta)$. When inserted into equations (16) and (17), such fits allow a prediction of how the clustering of pixels above a certain threshold temperature should depend on threshold if the signal is Gaussian and the noise is inhomogeneous.
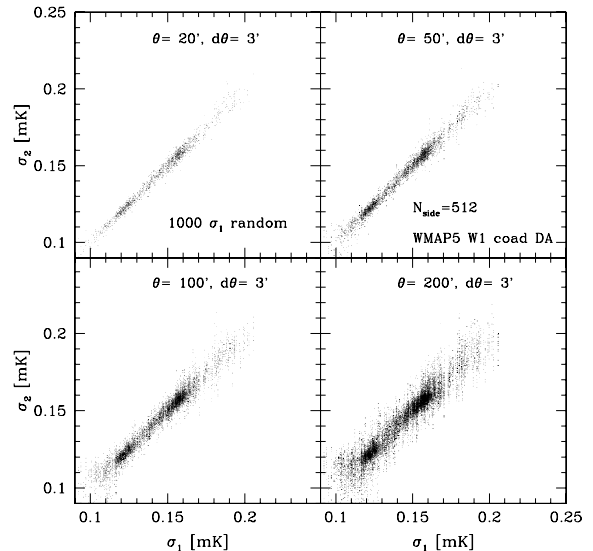

Figure 3. Joint distribution $p(\sigma_1, \sigma_2|\theta)$ at $N_{side} = 512$ resolution for four different choices of θ as indicated in the panels, from the *WMAP*5 W1 coadded channel.
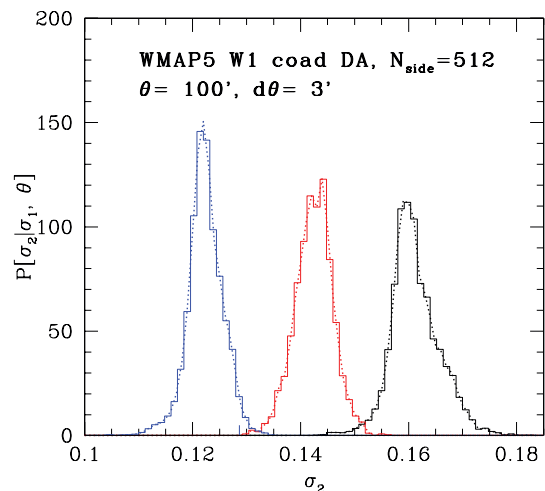

Figure 4. Examples of conditional probability distributions $p(\sigma_2|\sigma_1, \theta)$, when $\theta = 100$ arcmin, for the *WMAP*5 W1 coadded channel. The panel shows results for $N_{side} = 512$. Different sets of curves (spline fits) show the distribution of σ_2 for $\sigma_1 = 0.122, 0.142, 0.162$ mK, respectively.

3.3 Distribution of temperature

The histogram in Fig. 5 shows the distribution of temperature in the data, for the W1 coadded channel. For homogeneous noise, the predicted distribution would be given by convolving the expected signal (in this case, Gaussian with variance determined by smoothing the best-fitting power spectrum on the scale of a pixel) with that of the noise (Gaussian with average rms σ_N). For inhomogeneous noise, the predicted distribution (i.e. equation 1) is given by convolving the expected Gaussian signal with the noise of rms σ_n, and then weighting by the distribution of σ_n shown in Fig. 2. The dotted line in Fig. 5 shows a Gaussian with the same rms as the data. This fit has shorter tails than the data. While this may be indicating that the signal is non-Gaussian (in fact, the sample skewness of the temperature distribution is -0.01216 mK^3, and the sample excess
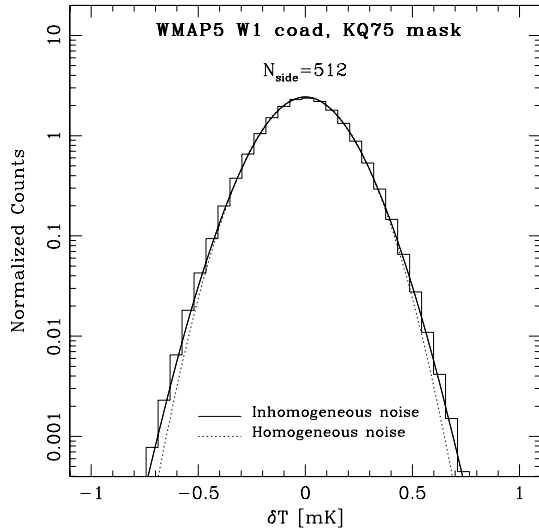
Figure 5. Distribution of temperature when $N_{side} = 512$ for the *WMAP*5 W1 channel (histogram). Solid line shows the expected distribution (equation 1) given the distribution of the noise. Dotted line is a Gaussian with the same rms as the data.

Figure 6. Number density of hot and cold pixels at $N_{side} = 512$, for the *WMAP*5 W1 channel. Points are measurements from the data. Dotted line is the theoretical prediction for homogeneous noise, and solid line includes inhomogeneity. Different temperature thresholds are considered, as explained in the main text.

kurtosis 0.12698 mK^4), the solid curve in Fig. 5 shows the predicted distribution when inhomogeneous noise effects are included: it provides substantially a better agreement with the measurements.

Nevertheless, the one-point distribution itself cannot rule out a priori the presence of a non-Gaussian signal, for reasons made explicit in Fang & Pando (1997); hence, it is not a suitable statistics to investigate departures from Gaussianity. This is also relevant for the detection of non-Gaussianity claimed by Jeong & Smoot (2007), where the one-point distribution was used. We also note that their equation (9) is missing one integration over the distribution of the noise (see again our equation 1 for comparison).

3.4 Pixel number density

The number density of pixels above (below) a given temperature threshold is simply obtained by multiplying the fraction of pixels above (below) the threshold D_t (equation 4) by the total number density after masking (i.e. the total number of pixels after masking over the 'available' or 'unmasked' area). If the noise were homogeneous then this prediction is rather straightforward: equation (4) simply reduces to erfc($\nu/\sqrt{2}$)/2, where $\nu = D_t/\sigma_D$. In practice, due to the inhomogeneity of the noise, one needs to integrate (4) numerically, using the distributions $p(\sigma)$ measured from the data (Fig. 2). The solid lines in Fig. 6 are the results of this integration, when accounting for inhomogeneous noise. Dotted lines are the theoretical predictions which assume homogeneous noise. Points in Fig. 6 show measurements from the *WMAP*5 W1 channel, for pixels above or below a threshold, where $|\nu| = 0.5, 1.0, 1.5, 2.0, 2.5$, respectively. Error bars are from a Poisson analysis. While the solid lines slightly improve the fits, significant departures still remain, especially at higher thresholds.

3.5 Two-point statistics above threshold

We have measured the correlation function of pixels above and below a threshold temperature from the *WMAP* 5-year coadded maps, for a range of thresholds. In each case, we measured the
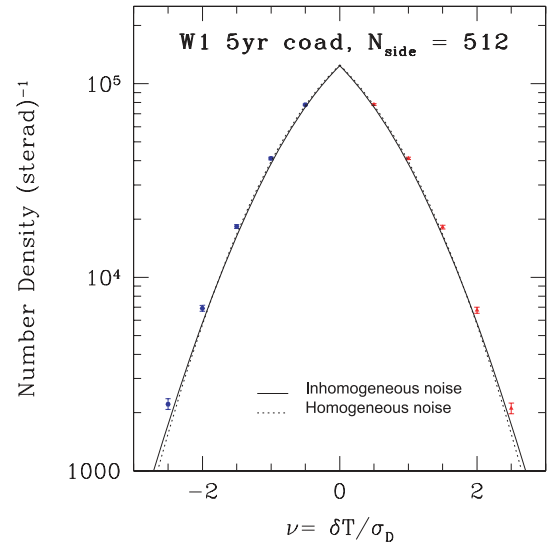
signal in two ways: one in which all pixels are treated equally and another in which the pixels are weighted by their temperature. We adopt here the standard estimator $1 + \xi(\theta) = DD(\theta)/RR(\theta)$ for the correlation function (Jensen & Szalay 1986), where $DD(\theta)$ and $RR(\theta)$ are the number of data and random pairs, respectively. In particular, the number of random pairs is computed by distributing random points on a unit sphere, and then by applying the same procedures (i.e. KQ75 masking and HEALPIX coordinate assignment) as for the data pipeline. For the weighted correlation estimates, the number of data pairs, $DD(\theta)$, is simply replaced by its temperature weighted counterpart, $WW(\theta)$. We also tested the Landy & Szalay (1993) and the Hamilton (1993) estimators, and found no significant differences in the calculations.

Figs 7 and 8 show an example of the results for pixels with $|\nu| = 0.25, 0.50, 0.75, 1.00, 1.25, 1.50$, respectively. In all panels, symbols show the measurements of hot and cold pixels at the fixed threshold; errors are from a Poisson analysis. Dotted curves in all the left-hand panels show the results based on homogeneous noise, solid curves in all the right-hand panels account for the fact that the noise is inhomogeneous (equations 12 and 13). Shaded areas are derived as explained in Appendix A (see also Hernández-Monteagudo et al. 2004), and represent the 1σ optimal variance errors.

Accounting for inhomogeneity significantly improves the fit to the data. However, discrepancies between the observed correlation functions and the theoretical predictions still remain, especially for pixels at higher thresholds, or at small angular scales. In particular, we note the interesting fact that hot and cold pixels cluster differently within the same temperature thresholds. This feature is also present in all the other *WMAP*5 channels (see Appendix B), but we find that our theory is always in good agreement with the clustering of cold pixels in the Q and V frequency bands, and only in slight disagreement with the hot patch clustering, especially for pixels at higher thresholds. Moreover, the fact that the *WMAP*5 data appear to be systematically stronger (weaker) at small (large) angular scales than the theoretical predictions, even at lower temperature thresholds (Figs 7 and 8) is particularly true in the W channel (see Fig. B4 for comparison). We suggest some possible interpretations
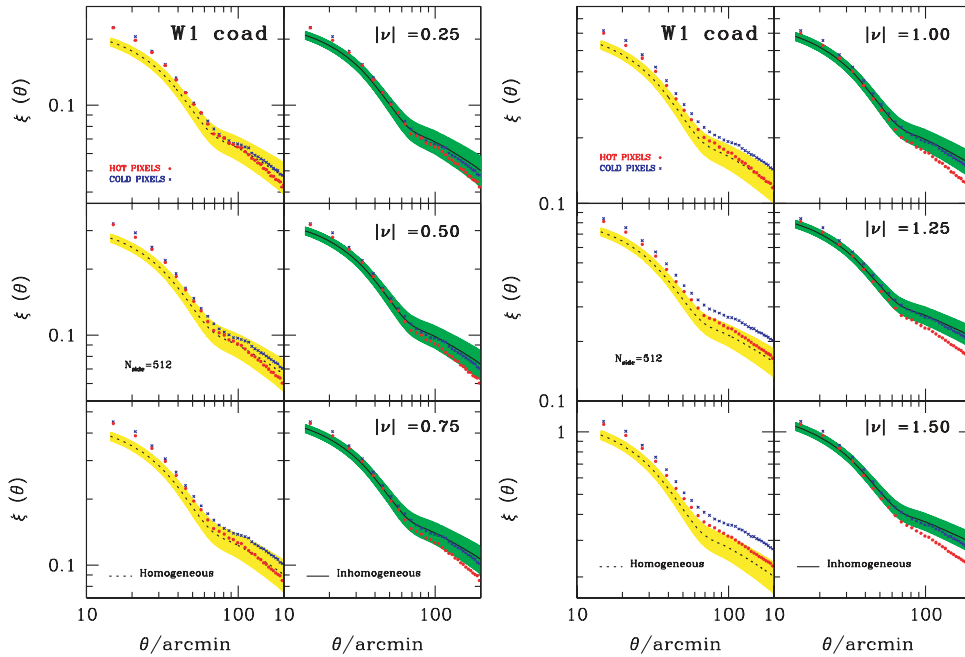
Figure 7. Unweighted correlation functions of pixels above threshold calculated from the *WMAP*5 W1 temperature field, at $N_{side} = 512$. A variety of pixel thresholds are considered, as indicated in the panels. Dotted curves in the left-hand panels show the predictions associated with Gaussian signal plus homogeneous noise, solid curves in the right-hand panels show the case of inhomogeneous noise. Points are measurements of the clustering of hot and cold pixels, at corresponding temperature thresholds. Shaded areas are the 1σ optimal variance errors.
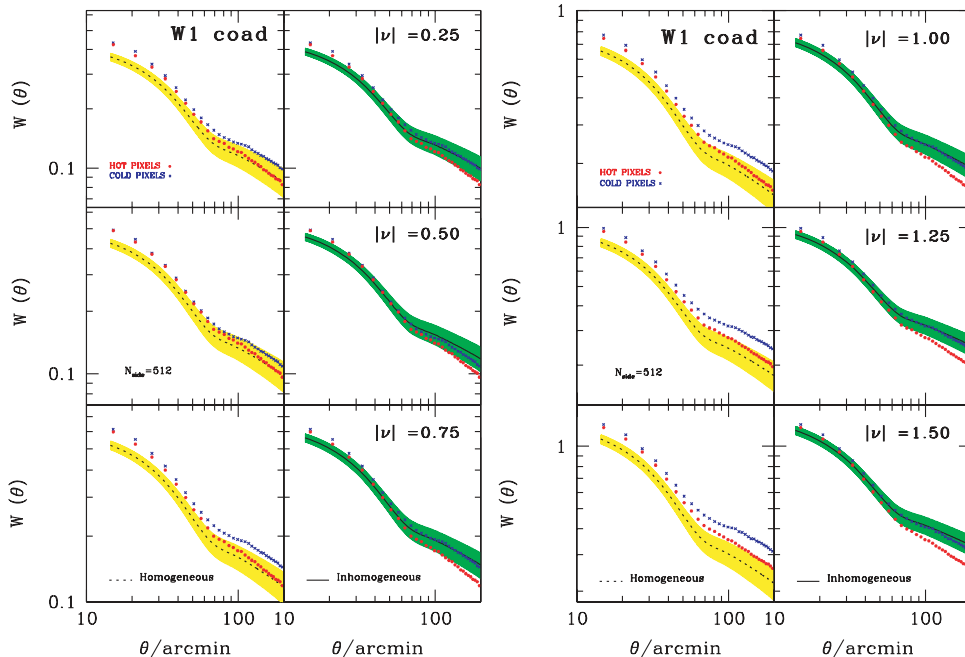
Figure 8. Same as Fig. 7, but for the weighted correlation functions.

in the Discussion section and in Appendix B, and present a more detailed investigation of this effect using realistic non-Gaussian mock simulations in a forthcoming paper.

While the detected trend may be a unique signature of primordial non-Gaussianity (i.e. a primordial non-Gaussianity would in fact enhance the clustering of the cold pixels and reduce that of the hot ones), we study the effect of smoothing the map next, and provide some other plausible explanations for these anomalies in the final section.

3.6 Effect of smoothing

We have investigated the effect of smoothing the *WMAP* 5-year maps with a Gaussian beam. In particular, we have tried different smoothing scales, corresponding to a full width at half-maximum (FWHM) of 30, 45, 60 and 75 arcmin, respectively. We have repeated the same analysis as for the unsmoothed maps, and characterized the number density and the clustering statistics of pixels above threshold.
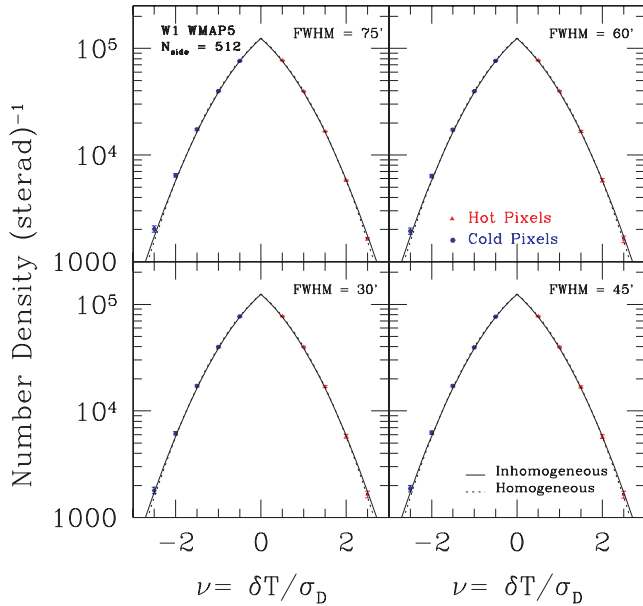
Figure 9. Number density of hot and cold pixels at $N_{side} = 512$, for the smoothed *WMAP*5 (W1 channel) maps. In each panel, points are measurements from data, dotted lines are the theoretical predictions for homogeneous noise, solid lines include inhomogeneity. From top to bottom and clockwise, the FWHM of the Gaussian beam is 75, 60, 45 and 30 arcmin, respectively.

Fig. 9 summarizes the results for the number density (W1 channel), after smoothing with different Gaussian beams. The number of pixels above or below the considered temperature threshold is reduced (a function of the smoothing scale), and measurements from the data and theoretical predictions appear now in agreement within about 1σ at the threshold levels considered.

Finally, we have characterized the clustering statistics and showed in Fig. 10 the case of inhomogeneous noise, for an arbitrary choice of the threshold ($|\nu| = 1.0$). The Gaussian smoothing is included in our theory via equations (24) and (25), in addition to the change of the noise variance distribution. After smoothing the map with a Gaussian beam, the pixel noise may be no longer independent among different pixels (i.e. $\langle n_1 n_2 \rangle \neq 0$). However, accounting for this contribution (equation 10) resulted in no significant difference, even at small angular scales. In fact, the average variance of the noise in the W1 channel is 0.0213 mK^2, which is about 0.32 per cent of the typical variance of the corresponding cosmological signal. Since the zero-level amplitude of the noise is already very low with respect to that of the signal, the mean amplitude of the correlated noise will be also very low. In addition to that, note that the *WMAP* mission has been designed to have uncorrelated pixel noise, and if such correlations arise when smoothing the maps their amplitude is expected to drop quickly with the smoothing scale.

When the smoothing scale is 75 arcmin, we find that the tension between data and theory is alleviated.

4 DISCUSSION

The observed distribution of temperatures in *WMAP*5 pixels is slightly non-Gaussian (Fig. 5). This departure from Gaussianity is not unexpected if the intrinsic signal is Gaussian but the noise distribution is inhomogeneous white noise (Figs 1 and 2). In fact, when accounting for inhomogeneous noise (Section 2), we find that the one-point statistics are substantially in better agreement with

the measurements. However, the predicted dependence of clustering on pixel height is not in good agreement with the data, even after accounting for the inhomogeneity of the noise (Figs 7 and 8). Although we found that an appropriate smoothing scale would be able to alleviate the discrepancy between data and measurements (Figs 9 and 10), other possible reasons for these discrepancies are as follows.

Masking procedure. In our analysis, we adopted the KQ75 mask, which allows for selective exclusions of bright portions of the sky (28 per cent pixel cut). Although this is rather a drastic cut and the mask was significantly improved with the *WMAP* 5-year data release (Hill et al. 2009), it may not completely account for all the Galactic foreground effects. However, cutting out all the Galactic plane ($|b| \leq 30°$ strip) and repeating our analysis resulted in no significant change. Edge effects due to pixels which lie very close to the mask could also affect our analysis.

Cold spot contamination. Inoue & Silk (2007) suggest that the presence of low-density regions in the southern Galactic cap could account for our anomalies, but restricting our analysis to $b \geq 30°$, the northern Galactic cap, resulted in no significant change.

Contamination by point sources. López-Caniego et al. (2007) detected 98 new sources (i.e. 26 per cent) not present in the *WMAP* 3-year catalogue. At higher frequencies, *WMAP* estimates neglect the deviations of the point spread function from a Gaussian shape, and carry out a blind search for sources. With the *WMAP* 5-year data release, the mask for point sources has been significantly improved (Wright et al. 2009), and other studies (Chen & Wright 2008; González-Nuevo et al. 2008) updated the point source catalogue. However, Massardi et al. (2009) recently provided a new version of the catalogue based on *WMAP*5 data and found new point sources (484 sources detected), carrying a complementary blind and non-blind approach. This may be important to our analysis, since even a very low-level contamination in the maps can produce spurious non-Gaussianities. In fact, we find some discrepancies at small angular scales (around 20 arcmin) especially in the *W* band, and their origin may be associated with extragalactic dust emission (one type of point-source contamination), which peaks at high frequencies. In a forthcoming study, we will be addressing the effect of contamination induced by point sources in more depth, using an updated version of the source catalogue and mock simulations.

Foreground subtraction contamination. Uncertainties in the external Foreground Template Model used for the foreground subtractions (Gold et al. 2009) may introduce anomalies at the percentage level. The template itself has noise, which may be correlated at small separations. This is a delicate issue, since Galactic foregrounds are non-Gaussian and anisotropic, and even low-level contamination in the maps can produce detectable non-Gaussianities (Park, Park & Ratra 2002; Naselsky et al. 2005; Kim, Naselsky & Christensen 2008). On the other side, it is also worth noting that recently Vio & Andreani (2008) showed that the benefits of using more sophisticated methods for foreground cleaning, such as the Harmonic Internal Linear Combination, are overestimated. We are also addressing the foreground subtraction systematics in a forthcoming study.

WMAP beam, window function, absolute calibration and pixel-noise uncertainties. Window functions were computed from the symmetrized beam profiles following the Hermite method in Page et al. (2003). A typical *WMAP* window function has an uncertainty
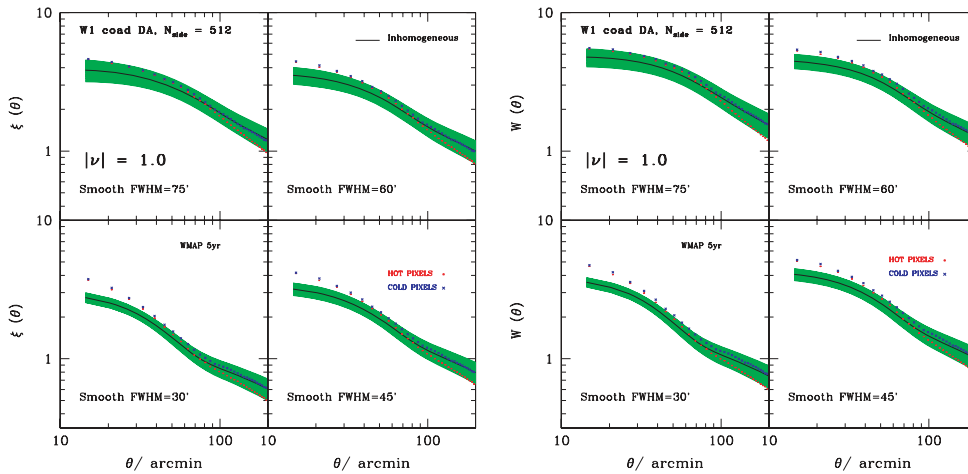
Figure 10. Unweighted (left-hand panel) and weighted (right-hand panel) correlation functions from the *WMAP*5 pixel–pixel temperature field smoothed at different scales, at $N_{side} = 512$, for the W1 channel. The pixel threshold considered is $|\nu| = 1.0$. In each panel, from top to bottom panels and clockwise, the FWHM of the Gaussian beam is, respectively, 75, 60, 45 and 30 arcmin. Solid curves show the case of inhomogeneous noise. Points are measurements of the clustering of hot and cold pixels, at corresponding temperature thresholds. Shaded areas are the 1σ optimal variance errors.

of 2–3 per cent (Hill et al. 2009), and these uncertainties add in quadrature in the cosmological analysis. Absolute calibration uncertainties in the 5-year *WMAP* data are estimated to be 0.5 per cent (Hinshaw et al. 2009). Recent studies (Groeneboom et al. 2009; Kathrine Wehus et al. 2009) have also pointed out that the noise levels of these maps are underestimated, and that there are some problems with the standard *WMAP* transfer functions as well. It may be that these facts play an important rule in our study (see also Colombo, Pierpaoli & Pritchard 2008).

Secondary anisotropies and phase transitions in the early Universe. Spurious non-Gaussianities could arise from secondary anisotropies, such as gravitational lensing, Sunyaev–Zel'dovich effect or Sachs–Wolfe effects (Babich & Pierpaoli 2008; Carbone et al. 2008). Phase transitions in the early Universe may also introduce a new source of non-Gaussianity (Silvestri & Trodden 2008). All these effects may be difficult to disentangle from a pure primordial non-Gaussian signal, even after a clear detection of primordial non-Gaussianity.

Real non-Gaussian signatures at small scales. A better understanding of all the previous points is necessary before we can claim that the signal we see is due to primordial non-Gaussianity. However, we found an interesting difference in the clustering of hot and cold pixels within the same temperature threshold level; this fact may be a unique signature of primordial non-Gaussianity. We present a detailed investigation of this feature in a forthcoming study. We finally note that, as this work was being referred, Hou, Banday & Gorski (2009) presented a frequentist analysis of the correlation functions of the local extrema, and also found inconsistency with Gaussian simulations plus differences in the clustering of hot and cold peaks – although comparison with their work is not direct since they considered bigger angular scales.

While seeking for primordial non-Gaussianity is at the moment a new frontier in cosmology, ongoing efforts are currently devoted to the characterization of non-Gaussian confusion effects, to reliable theoretical predictions of non-Gaussianity from models (see e.g. Boyle & Steinhardt 2008; Fergusson & Shellard 2008; Munshi & Heavens 2009), till the extraction of information from data (i.e.

Raeth et al. 2009; Gong et al. 2009) or the search for observational signatures of primordial non-Gaussianity imprinted in the large-scale structure of the Universe. Even a small degree of primordial non-Gaussianity can be a crucial probe of the inflationary dynamics or alternative universe models, hence studies of non-Gaussianity may eventually become a powerful and solid probe of ultrahigh energy physics and inflation.

We note that our model for the effects of inhomogeneous noise may be useful in other studies (see e.g. Yu & Lu 2008). Extending our formalism for inhomogeneous noise to peak rather than pixel statistics (e.g. Heavens & Sheth 1999; Heavens & Gupta 2001) is more complicated; this will complement numerical Monte Carlo analyses of this problem (Larson & Wandelt 2004; Tojeiro et al. 2006; Ayaita, Weber & Wetterich 2009; Hou et al. 2009), and is the subject of work in progress.

REFERENCES

Alishahiha M., Silverstein E., Tong D., 2004, Phys. Rev. D, 70, 123505
Arkani-Hamed N., Creminelli P., Mukohyama S., Zaldarriaga M., 2004, J. Cosmol. Astropart. Phys., 4, 1
Ayaita Y., Weber M., Wetterich C., 2009, preprint (arXiv:0905.3324)
Babich D., Pierpaoli E., 2008, Phys. Rev. D, 77, 123011
Bartolo N., Komatsu E., Matarrese S., Riotto A., 2004, Phys. Rep., 402, 103
Bond J. R., Efstathiou G., 1987, MNRAS, 226, 655
Boyle L., Steinhardt P. J., 2008, preprint (arXiv:0810.2787)
Brandenberger R. H., 2008, preprint (arXiv:0808.0746)
Buchbinder E. I., Khoury J., Ovrut B. A., 2008, Phys. Rev. Lett., 100, 171302
Cabella P., Liguori M., Hansen F. K., Marinucci D., Matarrese S., Moscardini L., Vittorio N., 2005, MNRAS, 358, 684
Carbone C., Verde L., Matarrese S., 2008, ApJ, 684, L1
Chen X., 2005, Phys. Rev. D, 72, 123518
Chen G., Szapudi I., 2006, ApJ, 647, L87
Chen X., Wright E. L., 2008, ApJ, 694, 222
Chen X., Hu B., Huang M.-X., Shiu G., Wang Y., 2009, preprint (arXiv:0905.3494)
Chiang L.-Y., Naselsky P. D., Coles P., 2007, ApJ, 664, 8
Colombo L. P. L., Pierpaoli E., Pritchard J. R., 2008, preprint (arXiv:0811.2622)
Creminelli P., Senatore L., 2007, J. Cosmol. Astropart. Phys., 11, 10
Creminelli P., Senatore L., Zaldarriaga M., Tegmark M., 2007, J. Cosmol. Astropart. Phys., 3, 5
Crociani D., Moscardini L., Viel M., Matarrese S., 2009, MNRAS, 394, 133
Cruz M., Tucci M., Martínez-González E., Vielva P., 2006, MNRAS, 369, 57
Curto A., Martinez-Gonzalez E., Mukherjee P., Barreiro R. B., Hansen F. K., Liguori M., Matarrese S., 2009, MNRAS, 393, 615
Dalal N., Doré O., Huterer D., Shirokov A., 2008, Phys. Rev. D, 77, 123514
Desjacques V., Seljak U., Iliev I. T., 2009, MNRAS, 396, 85
Dickinson C. et al., 2009, preprint (arXiv:0903.4311)
Diego J. M., Cruz M., Gonzalez-Nuevo J., Maris M., Ascasibar Y., Burigana C., 2009, preprint (arXiv:0901.4344)
Dunkley J. et al., 2009, ApJS, 180, 306
Dvali G., Gruzinov A., Zaldarriaga M., 2004, Phys. Rev. D, 69, 083505
Fang L.-Z., Pando J., 1997, preprint (astro-ph/9701228)
Fergusson J. R., Shellard E. P. S., 2008, preprint (arXiv:0812.3413)
Górski K. M. et al., 1999, in Banday A. J., Sheth R. K., da Costa L. A. V., eds, Proc. MPA/ESO Conf., Evolution of Large-Scale Structure: From Recombination to Garching. European Southern Observatory, Garching, p. 37
Gold B. et al., 2009, ApJS, 180, 265
Gong Y., Wang X., Zheng Z., Chen X., 2009, preprint (arXiv:0904.4257)
González-Nuevo J., Massardi M., Argüeso F., Herranz D., Toffolatti L., Sanz J. L., López-Caniego M., de Zotti G., 2008, MNRAS, 384, 711
Gott J. R., Colley W. N., Park C.-G., Park C., Mugnolo C., 2007, MNRAS, 377, 1668
Gott J. R. I. et al., 2008, ApJ, 675, 16
Gott J. R. I., Choi Y.-Y., Park C., Kim J., for the SDSS Collaboration, 2009, ApJ, 695, L45
Groeneboom N. E., Eriksen H. K., Gorski K., Huey G., Jewell J., Wandelt B., 2009, preprint (arXiv:0904.2554)
Grossi M., Branchini E., Dolag K., Matarrese S., Moscardini L., 2008, MNRAS, 390, 438
Hamilton A. J. S., 1993, ApJ, 417, 19
Hansen F. K., Banday A. J., Gorski K. M., Eriksen H. K., Lilje P. B., 2008, preprint (arXiv:0812.3795)
Heavens A. F., Gupta S., 2001, MNRAS, 324, 960
Heavens A. F., Sheth R. K., 1999, MNRAS, 310, 1062
Hernández-Monteagudo C., Kashlinsky A., Atrio-Barandela F., 2004, A&A, 413, 833
Hikage C., Coles P., Grossi M., Moscardini L., Dolag K., Branchini E., Matarrese S., 2008a, MNRAS, 385, 1613
Hikage C., Matsubara T., Coles P., Liguori M., Hansen F. K., Matarrese S., 2008b, MNRAS, 389, 1439

Hill R. S. et al., 2009, ApJS, 180, 246
Hinshaw G. et al., 2003, ApJS, 148, 135
Hinshaw G. et al., 2007, ApJS, 170, 288
Hinshaw G. et al., 2009, ApJS, 180, 225
Hou Z., Banday A. J., Gorski K. M., 2009, MNRAS, 396, 1273
Inoue K. T., Silk J., 2007, ApJ, 664, 650
Jarosik N. et al., 2007, ApJS, 170, 263
Jensen L. G., Szalay A. S., 1986, ApJ, 305, L5
Jeong D., Komatsu E., 2009, preprint (arXiv:0904.0497)
Jeong E., Smoot G. F., 2007, preprint (arXiv:0710.2371)
Kamionkowski M., Verde L., Jimenez R., 2009, J. Cosmol. Astropart. Phys., 1, 10
Kang X., Norberg P., Silk J., 2007, MNRAS, 376, 343
Kashlinsky A., Hernández-Monteagudo C., Atrio-Barandela F., 2001, ApJ, 557, L1
Kathrine Wehus I., Ackerman L., Eriksen H. K., Groeneboom N. E., 2009, preprint (arXiv:0904.3998)
Kim J., Naselsky P., Christensen P. R., 2009, Phys. Rev. D, 79, 023003
Knox L., 1995, Phys. Rev. D, 52, 4307
Komatsu E. et al., 2009, ApJS, 180, 330
Landy S. D., Szalay A. S., 1993, ApJ, 412, 64
Larson D. L., Wandelt B. D., 2004, ApJ, 613, L85
Lehners J.-L., Steinhardt P. J., 2008, Phys. Rev. D, 77, 063533
Li T.-P., Liu H., Song L.-M., Xiong S.-L., Nie J.-Y., 2009, preprint (arXiv:0905.0075)
Ling Y., Wu J.-P., 2009, Phys. Lett. B, 675, 151
López-Caniego M., González-Nuevo J., Herranz D., Massardi M., Sanz J. L., De Zotti G., Toffolatti L., Argüeso F., 2007, ApJS, 170, 108
Lo Verde M., Miller A., Shandera S., Verde L., 2008, J. Cosmol. Astropart. Phys., 4, 14
Lyth D. H., Ungarelli C., Wands D., 2003, Phys. Rev. D, 67, 023503
Lyth D. H., Riotto A., 2006, Phys. Rev. Lett., 97, 121301
McAllister L., Silverstein E., 2008, Gen. Relativ. Gravit., 40, 565
McDonald P., Seljak U., 2008, preprint (arXiv:0810.0323)
Massardi M., López-Caniego M., González-Nuevo J., Herranz D., De Zotti G., Sanz J. L., 2009, MNRAS, 392, 733
Matarrese S., Verde L., 2008, ApJ, 677, L77
Munshi D., Heavens A., 2009, preprint (arXiv:0904.4478)
Naselsky P., Chiang L.-Y., Olesen P., Novikov I., 2005, Phys. Rev. D, 72, 063512
Naselsky P. D., Christensen P. R., Coles P., Verkhodanov O., Novikov D., Kim J., 2007, preprint (arXiv:0712.1118)
Nolta M. R. et al., 2009, ApJS, 180, 296
Page L. et al., 2003, ApJS, 148, 39
Park C., Colley W. N., Gott J. R. I., Ratra B., Spergel D. N., Sugiyama N., 1998, ApJ, 506, 473
Park C., Gott J. R. I., Choi Y. J., 2001, ApJ, 553, 33
Park C.-G., Park C., Ratra B., 2002, ApJ, 568, 9
Park C. et al., 2005, ApJ, 633, 11
Pietrobon D., Cabella P., Balbi A., de Gasperis G., Vittorio N., 2009a, MNRAS, 396, 1682
Pietrobon D., Cabella P., Balbi A., Crittenden R., de Gasperis G., Vittorio N., 2009b, preprint (arXiv:0905.3702)
Pillepich A., Porciani C., Matarrese S., 2007, ApJ, 662, 1
Pillepich A., Porciani C., Hahn O., 2008, preprint (arXiv:0811.4176)
Räth C., Schuecker P., Banday A. J., 2007, MNRAS, 380, 466
Räth C., Morfill G. E., Rossmanith G., Banday A. J., Górski K. M., 2009, Phys. Rev. Lett., 102, 131301
Rossmanith G., Raeth C., Banday A. J., Morfill G., 2009, preprint (arXiv:0905.2854)
Seery D., Lidsey J. E., 2005, J. Cosmol. Astropart. Phys., 9, 11
Seery D., Hidalgo J. C., 2006, J. Cosmol. Astropart. Phys., 7, 8
Seljak U., 2009, Phys. Rev. Lett., 102, 021302
Senatore L., Tassev S., Zaldarriaga M., 2008, preprint (arXiv:0812.3658)
Senatore L., Smith K. M., Zaldarriaga M., 2009, preprint (arXiv:0905.3746)
Slosar A., Hirata C., Seljak U., Ho S., Padmanabhan N., 2008, J. Cosmol. Astropart. Phys., 8, 31
Silvestri A., Trodden M., 2008, preprint (arXiv:0811.2176)

Song H., Lee J., 2008, preprint (arXiv:0811.1339)

Spergel D. N. et al., 2007, ApJS, 170, 377

Tojeiro R., Castro P. G., Heavens A. F., Gupta S., 2006, MNRAS, 365, 265

Viel M., Branchini E., Dolag K., Grossi M., Matarrese S., Moscardini L., 2009, MNRAS, 393, 774

Vielva P., Wiaux Y., Martínez-González E., Vandergheynst P., 2007, MNRAS, 381, 932

Vielva P., Sanz J. L., 2009, MNRAS, in press (arXiv:0812.1756)

Vio R., Andreani P., 2008, preprint(arXiv:0811.4277)

Yadav A. P. S., Wandelt B. D., 2008, Phys. Rev. Lett., 100, 181301

Yu B., Lu T., 2008, Phys. Rev. D, 78, 063008

Wright E. L. et al., 2009, ApJS, 180, 283

APPENDIX A: ACCOUNTING FOR FINITE BIN-SIZE EFFECTS

We estimate the uncertainties in the correlation functions above threshold from the optimal variance limit, containing cosmic variance, instrumental noise and finite bin-size effects.

In more detail, the ultimate accuracy with which the CMB power spectrum can be determined at each l is given by (Knox 1995)

$$\sigma_{OV}^2(l) = \sqrt{\frac{2}{(2l+1)f_{sky}}}\left[C_l + \frac{4\pi\sigma_N^2}{N\,W_l^{WMAP}}\right] \equiv \Delta C_l, \quad (A1)$$

where N is the number of pixels, σ_N the average pixel noise, W_l^{WMAP} is the *WMAP* window function and f_{sky} is the fraction of the sky covered by the experiment. The uncertainty in the angular correlation function for narrow bins in θ is then (Hernández-Monteagudo et al. 2004)

$$\sigma_{C(\theta)}^2 \equiv \Delta C(\theta) = \left[\sum_l\left|\frac{\partial C(\theta)}{\partial C_l}\right|^2 \Delta C_l^2\right]^{1/2}$$

$$= \left\{\sum_l \frac{(2l+1)}{8\pi^2 f_{sky}}|P_l^0(\cos\theta)|^2(W^{WMAP}W^{smooth})^2\right.$$

$$\left.\times\left[\frac{2\pi C_l^\star}{l(l+1)} + \frac{\Omega_{pix}\sigma_N^2}{W^{WMAP}}\right]^2\right\}^{1/2}, \quad (A2)$$

where $C_l^\star = l(l+1)\,C_l/2\pi$ and W^{smooth} is the additional smoothing due to finite pixel size, mask influence and an optional Gaussian beam.

However, in practice $C(\theta)$ is not measured at a point, but smeared out over a region of size $\Delta\theta$. In the limit of large l and small θ, $P_l(\cos\theta) \sim J_0[(l+1/2)\theta]$ (Bond & Efstathiou 1987). If the bin size is not infinitesimal, one must replace:

$$J_0[(l+1/2)\theta] \rightarrow \frac{2}{\left(t_{max}^2 - t_{min}^2\right)}\int_{t_{min}}^{t_{max}} J_0[(l+1/2)t]\,t\,dt$$

$$= \frac{2[t_{max}J_1(kt_{max}) - t_{min}J_1(kt_{min})]}{k(t_{max}^2 - t_{min}^2)}, \quad (A3)$$

where $t_{min} = \theta - \Delta\theta/2$ and $t_{max} = \theta + \Delta\theta/2$. This expression should then substitute $P_l(\cos\theta) \sim J_0[(l+1/2)\theta]$ in (A2), to give $\sigma_{C_{\Delta\theta}(\theta)}^2 = \Delta C_{\Delta\theta}(\theta)$. The uncertainties in the correlation function above threshold are finally derived from

$$\sigma_{\xi_\nu(\theta)}^2 = \Delta\xi_\nu(\theta) = \left|\frac{\partial\xi_\nu(\theta)}{\partial C(\theta)}\right|\Delta C_{\Delta\theta}(\theta). \quad (A4)$$

APPENDIX B: RESULTS FOR ALL THE OTHER *WMAP* 5-YEAR DIFFERENCING ASSEMBLIES

We have inspected all the *WMAP* 5-year channels (*W* band at 94 GHz; *V* band at 61 GHz; *Q* band at 41 GHz), and performed the same analysis described in the main text for each single DA. For this study, it is ideal to consider individual DA rather than their combinations, as *WMAP* beams and noise properties are well defined within each single DA. Fig. B1 shows the distributions of the rms noise values for all the DAs considered; note the characteristic bimodality of these histograms presents in all the channels. Fig. B2 shows the distributions of temperatures in the data at different frequencies. Dotted lines in the figure are Gaussians with the same rms as data, solid curves show the predicted distributions when inhomogeneous noise effects are included. Departures from the Gaussian fits are more significant in the W frequency range. Fig. B3 shows the number density of pixels above (below) different temperature thresholds. Dotted lines are theoretical predictions with homogeneous noise, and solid lines include inhomogeneity. Points are measurements from all the *WMAP*5 DAs. Finally, Fig. B4 highlights
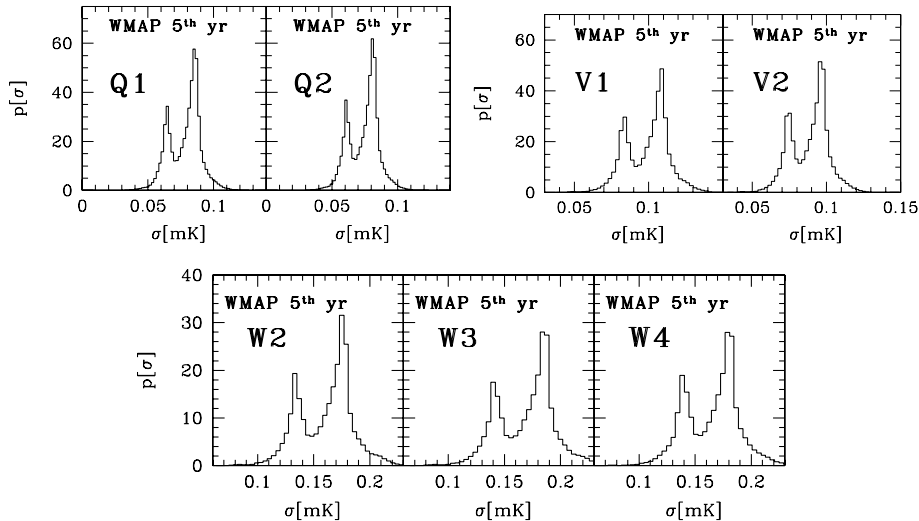

Figure B1. Distributions of the rms noise per pixel at $N_{side} = 512$ for the 5-year coadded *WMAP* data, after application of the KQ75 mask. From top to bottom and left to right, the various DAs are, respectively, Q1 and Q2 (the 41 GHz channel), V1 and V2 (the 61 GHz channel) and W2, W3, W4 (the 94 GHz channel).
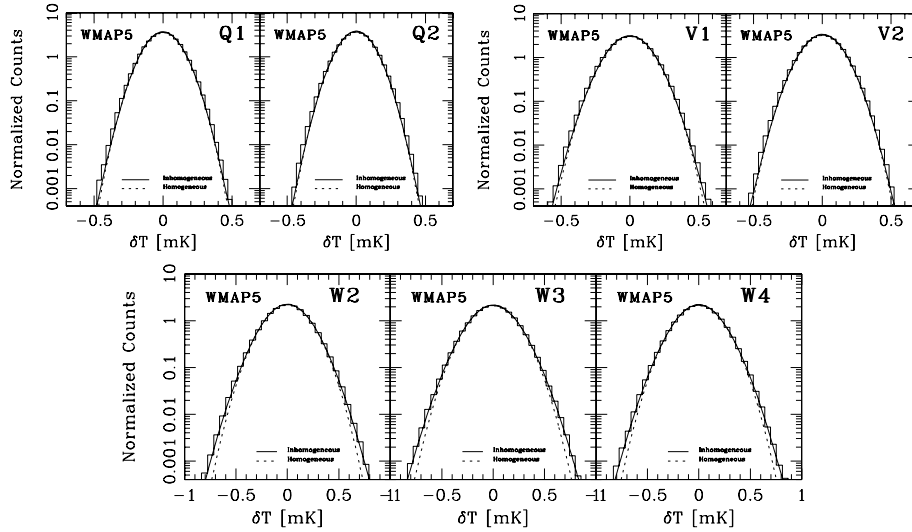
Figure B2. Distribution of temperatures when $N_{side} = 512$ (histograms). Solid lines in all panels show the expected distributions (equation 1) given the corresponding distributions of the noise. Dotted lines are Gaussians, with the same rms as the data. From top to bottom and left to right, the various DAs are, respectively, Q1, Q2, V1, V2, W2, W3, W4.
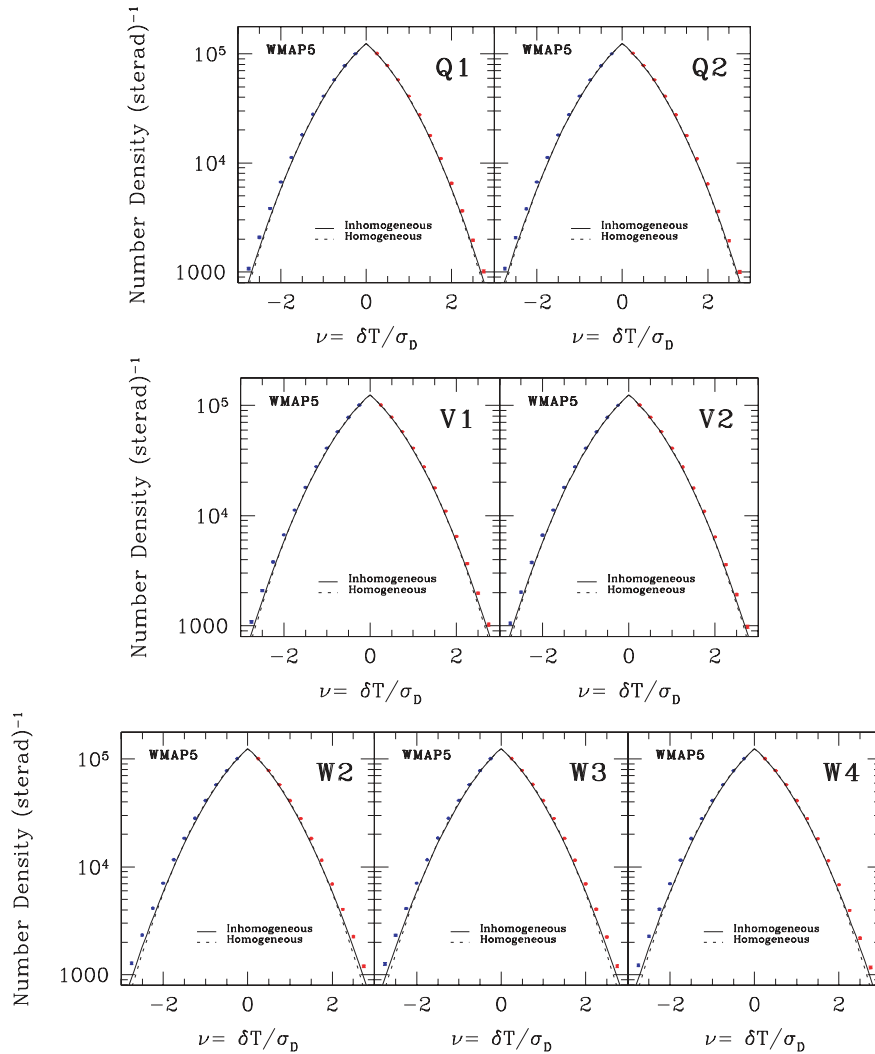
Figure B3. Number densities of hot and cold pixels at $N_{side} = 512$, for the WMAP5 individual channels. Points are measurements from the data. Dotted lines in all the panels are theoretical predictions for homogeneous noise, solid lines include inhomogeneity. From top to bottom and from left to right, the various DAs are, respectively, Q1, Q2, V1, V2, W2, W3, W4.
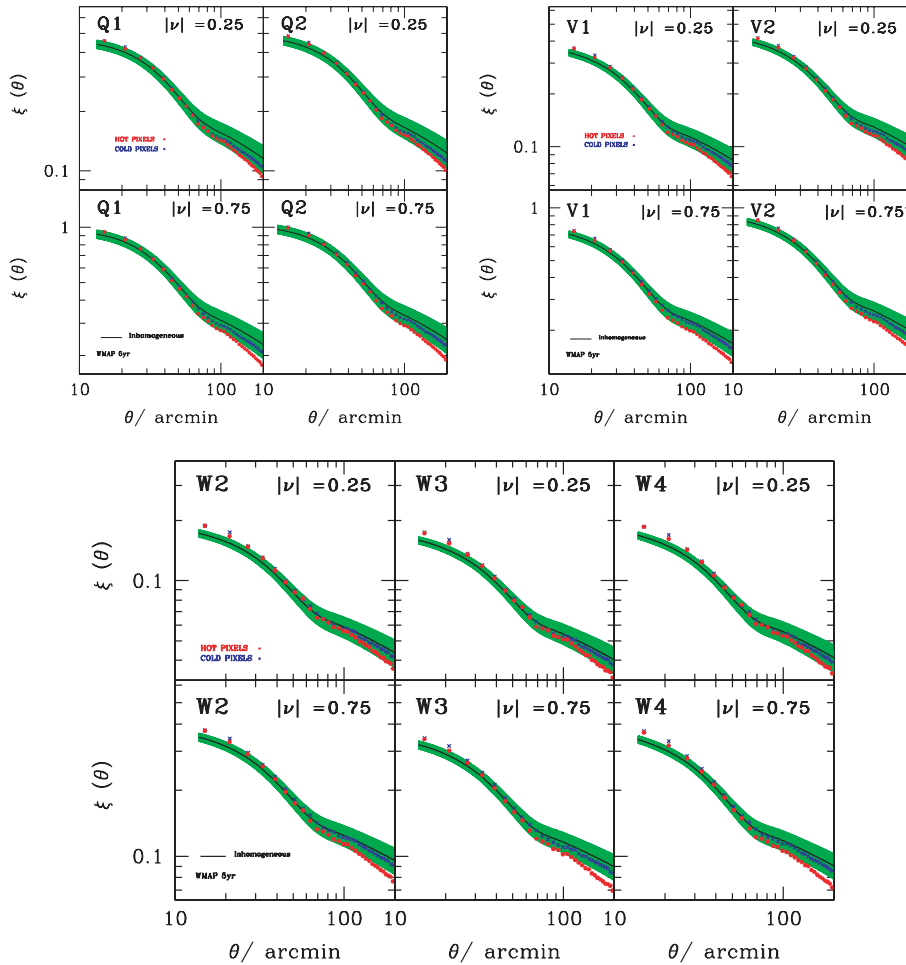
Figure B4. Examples of unweighted correlation functions from the WMAP5 pixel–pixel temperature field, at $N_{side} = 512$. Two pixel thresholds are considered ($|\nu| = 0.25$ and 0.75), as indicated in the panels. Solid curves in all panels show the predictions associated with Gaussian signal plus inhomogeneous noise. Points are measurements of the clustering of hot and cold pixels, at corresponding temperature thresholds. Shaded areas are the 1σ optimal variance errors. From top to bottom and from left to right, the various DAs are, respectively, Q1, Q2, V1, V2, W2, W3, W4.

some examples of the unweighted correlation functions from the *WMAP*5 pixel–pixel temperature fields, at $N_{side} = 512$. Two pixel thresholds are considered ($|\nu| = 0.25$ and 0.75), as indicated in the panels. Solid curves show the predictions associated with Gaussian signal plus inhomogeneous noise. Points are measurements of the clustering of hot and cold pixels at corresponding temperature thresholds, and shaded areas are the 1σ optimal variance errors. Essentially, we find that the difference in clustering between hot and cold pixels is still present in all the other DAs. However, our theory is always in good agreement with the clustering of cold pixels, and in slight disagreement with that of the hot ones, both in the Q and in

the V channels. Therefore, the 94 GHz frequency (*W* band) seems to be the most discrepant one, with respect to our theoretical predictions. In particular, we checked our small-scale theory expectations against *WMAP* mock measurements from simulations with identical beam and noise properties, and found full consistency. Hence, we suggest that those small-scale discrepancies may be due to extragalactic dust emission (one type of point-source contamination), which has a peak at high frequencies and is not accounted in our analysis.

This paper has been typeset from a TeX/LaTeX file prepared by the author.